The Astrophysical Journal, 929:37 (7pp), 2022 April 10 https://doi.org/10.3847/1538-4357/ac5894
© 2022. The Author(s). Published by the American Astronomical Society.
OPEN ACCESS

Is There an Enormous Cold Front at the Virial Radius of the Perseus Cluster?

S. A. Walker[1], M. S. Mirakhor[1], J. ZuHone[2], J. S. Sanders[3], A. C. Fabian[4], and P. Diwanji[1]
[1] Department of Physics and Astronomy, University of Alabama in Huntsville, Huntsville, AL 35899, USA; stephen.walker@uah.edu
[2] Harvard-Smithsonian Center for Astrophysics, 60 Garden Street, Cambridge, MA 02138, USA
[3] Max-Planck-Institute fur extraterrestrische Physik, D-85748 Garching, Germany
[4] Institute of Astronomy, Madingley Road, Cambridge, CB3 0HA, UK
Received 2020 June 24; revised 2022 February 18; accepted 2022 February 23; published 2022 April 11

Abstract

We present new XMM-Newton observations extending the mosaic of the Perseus cluster out to the virial radius to the west. Previous studies with ROSAT have reported a large excess in surface brightness to the west, possibly the result of large-scale gas sloshing. In our new XMM-Newton observations we have found two X-ray surface brightness edges at 1.2 and 1.7 Mpc to the west. The temperature measurements obtained with Suzaku data indicate that the temperature increases sharply at each edge, consistent with what would be expected from cold fronts. However the the XMM-Newton data are affected by stray light, which at present is a poorly understood source of systematic error that can also lead to curved features in X-ray images. To test our results, we compared our X-ray surface brightness profile with that obtained from ROSAT PSPC data. While the edge at 1.2 Mpc is confirmed by ROSAT PSPC, the ROSAT data quality is insufficient to confirm the outer edge at 1.7 Mpc. Further observations with future X-ray telescopes will be needed to confirm the existence of the outer edge at 1.7 Mpc. By comparing with numerical simulations, we find that these large cold fronts require a large impact parameter, and low-mass ratio mergers that can produce fast gas motions without destroying the cluster core.

Unified Astronomy Thesaurus concepts: Galaxy clusters (584); Intracluster medium (858); Perseus Cluster (1214); X-ray astronomy (1810); High energy astrophysics (739)

1. Introduction

Cold fronts produced by gas sloshing are commonly seen in the central cores of relaxed cool core galaxy clusters (see Markevitch & Vikhlinin 2007; Zuhone & Roediger 2016 for reviews), where the high surface brightness allows them to be easily resolved. At these cold fronts, the X-ray surface brightness and gas density drops sharply, while the temperature of the gas rises sharply, the opposite of what occurs for a shock.

The cold fronts in cluster cores have extremely narrow widths, smaller than the Coulomb mean free path, meaning that processes such as diffusion, conduction, and the onset of hydrodynamic instabilities have been heavily suppressed. Magnetic draping, in which the magnetic field is amplified at the cold front edge, is one mechanism believed to be operating to maintain the sharpness of the cold fronts (Lyutikov 2006; Asai et al. 2007; Dursi 2007; ZuHone et al. 2011).

These cold fronts are believed to be formed due to the sloshing of the cold cluster core as it responds to the gravitational disturbance created by an infalling subcluster's dark matter halo during an off-axis minor merger, as has been simulated by, for example, Tittley & Henriksen (2005), Ascasibar & Markevitch (2006), Roediger et al. (2011), and ZuHone et al. (2011). These simulations predict that the geometric features of older cold fronts should propagate outwards into the lower pressure regions of the cluster as they age, producing a characteristic spiral pattern of alternating cold fronts on opposite sides of the cluster at an ever greater distance from the cluster core. Exactly how far out this process can operate is uncertain, as the X-ray surface brightness decreases rapidly with radius in galaxy clusters, making detailed studies of sloshing into the cluster outskirts challenging (Walker et al. 2019).

One remarkable recent development in the study of cold fronts is the discovery of large-scale cold fronts reaching out to very large radii, far outside the cooling radius. In the Perseus cluster, Simionescu et al. (2012) and Walker et al. (2018) have found a cold front 700 kpc from the core to the east (nearly half the virial radius), using XMM and Chandra data. Perseus displays the characteristic sloshing spiral pattern of alternating cold fronts on either side of the cluster, extending from the sloshing activity in the core (Walker et al. 2017; Sanders et al. 2020) into the cluster outskirts. Similar large-scale cold fronts reaching out to $\sim 0.5 r_{200}$ have since been found in just a handful of other clusters, all at much higher redshifts: A2142 (Rossetti et al. 2013), RXJ 2014.8-2430 (Walker et al. 2014), and A1763 (Douglass et al. 2018). In all of these systems, there is a large-scale spiral pattern of concentric cold fronts on opposite sides of the cluster at increasing radii, suggesting that the structure is one continuous outwardly moving sloshing motion.

These large-scale cold fronts are much older than the cold fronts commonly found in cluster cores, as they have risen outwards and grown with time. They are over an order of magnitude further out from the core, and so if we assume a constant velocity, would be expected to be an order of magnitude older. Based on numerical simulations of rising cold fronts (ZuHone et al. 2011), the age of the cold front to the east at 700 kpc from Perseus's core explored in Walker et al. (2018) should be around 5 Gyr, while the age of the cold front that has reached the virial radius is expected to be at least 9 Gyr. Because of this, diffusion processes will have had much longer to broaden the cold front edge, while instabilities such as Kelvin–Helmholtz instabilities (which we have found in

Original content from this work may be used under the terms of the Creative Commons Attribution 4.0 licence. Any further distribution of this work must maintain attribution to the author(s) and the title of the work, journal citation and DOI.

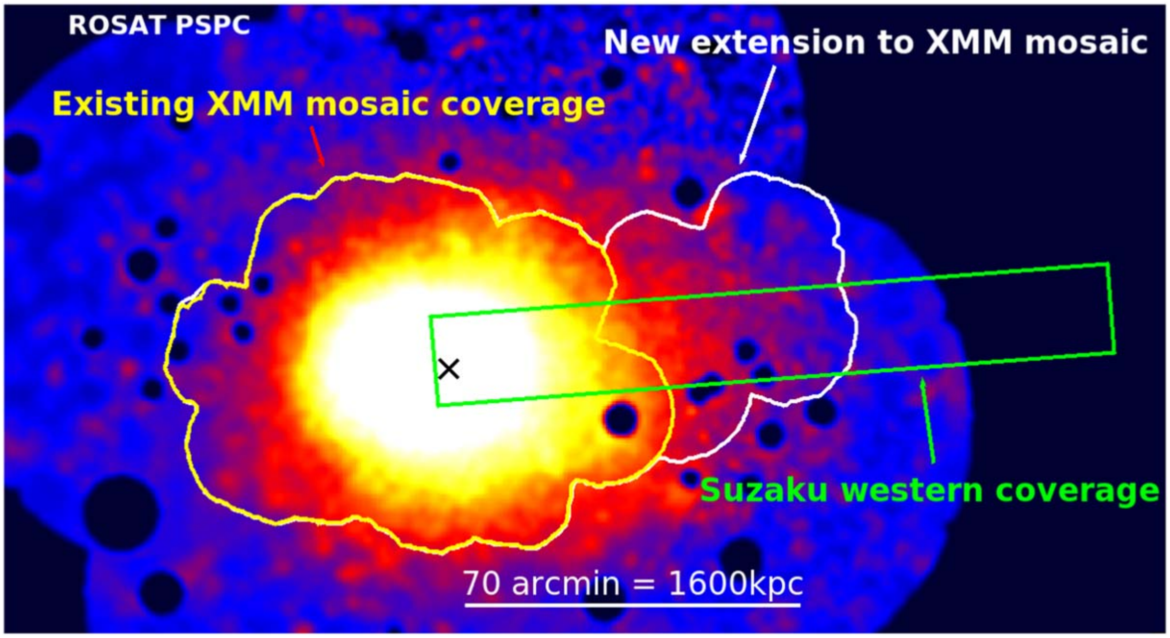

Figure 1. Large area, shallow ROSAT PSPC mosaic of the Perseus cluster. Overlaid on this is the field that XMM-Newton has covered previously (yellow contour), which we extend with our new observations toward the west (the white contour). The Suzaku coverage to the west is shown by the green area. The location of the core is donated by the black cross.

observations closer to the core; Walker et al. 2017) will have had longer to grow. We would therefore expect the broadening and substructure behind large-scale cold fronts to be significantly more evolved than that behind young cold fronts in cluster cores, and consequently easier to resolve spatially.

As cold fronts rise from the core to the outskirts they pass through different strata of the intracluster medium (ICM), which are expected to have different dominating physics. In the outskirts the physics of the ICM begins to be dominated by the accretion of gas onto the cluster from large-scale structure filaments and infalling subgroups. Turbulence and bulk motions from the ongoing formation of the cluster are expected from simulations (Lau et al. 2009) to increase in the outskirts. The rising cold front therefore experiences vastly different areas of the ICM as it grows, which will have an influence on the broadening of the cold front and the development of the structure behind it.

Simionescu et al. (2012) also found evidence from the mosaicked ROSAT PSPC data of Perseus that the sloshing spiral continued even further out to the west, extending out to nearly the virial radius ($r_{200} = 1800$ kpc $= 80'$ for Perseus; Urban et al. 2014). However the low effective area, and large off-axis point-spread function (PSF) of ROSAT made it impossible to determine whether this large excess in X-ray surface brightness to the west lay behind a cold front.

To remedy this, in AO17 we extended the XMM mosaic to reach out to the virial radius in a narrow strip to the west of Perseus to see if there is a cold front there.

Many outstanding questions remain about the way cold fronts evolve out to large radii. How far out can magnetic draping continue to suppress transport processes, and are we beginning to see this process break down? At some point in the cluster outskirts the cluster magnetic field must interact with that of the surrounding cosmic web filaments (Walker et al. 2019). These new XMM-Newton observations allow us to probe cluster astrophysics into extreme, previously unexplored regimes, providing crucial insights into the interface between clusters and the surrounding cosmic web.

In this paper we present these new XMM observations. We use a standard ΛCDM cosmology with $H_0 = 70$ km s^{-1} Mpc^{-1}, $\Omega_M = 0.3$, $\Omega_\Lambda = 0.7$. All errors unless otherwise stated are at the 1σ level.

2. Data

Figure 1 shows the wide-scale ROSAT PSPC mosaic image of Perseus. Over this we plot the existing regions covered by XMM (the yellow contour) and the region covered by our new extension of the mosaic reaching out to the virial radius to the west (white contour). This new XMM coverage to the west extends over the surface brightness excess found in Simionescu et al. (2012). We also show the Suzaku coverage in this western direction (green contour). The other seven strips of the Suzaku mosaic are not shown as none of them overlap with the new XMM data.

2.1. XMM-Newton Image Analysis

The XMM-Newton observations used are tabulated in Table 1, ordered with the latest observations at the top. Our new observations to extend the mosaic out to the virial radius to the west are 0820720101, 08207202101, 08207201301, and 0820720401.

All of the XMM observations were reduced using the XMM extended source analysis software (Snowden et al. 2008). The images and exposure maps were extracted in the 0.7–1.2 keV band (which has been found to maximize the signal to noise in the outskirts by, e.g., Tchernin et al. 2016) using MOS-SPECTRA and PN-SPECTRA, while particle background images were produced using MOS-BACK and PN-BACK. Residual soft proton contamination was modeled using spectral fitting and images were produced using the task PROTON. Point sources were identified using CHEESE (and also using the Chandra tool WAVDETECT) and removed. The resulting background-

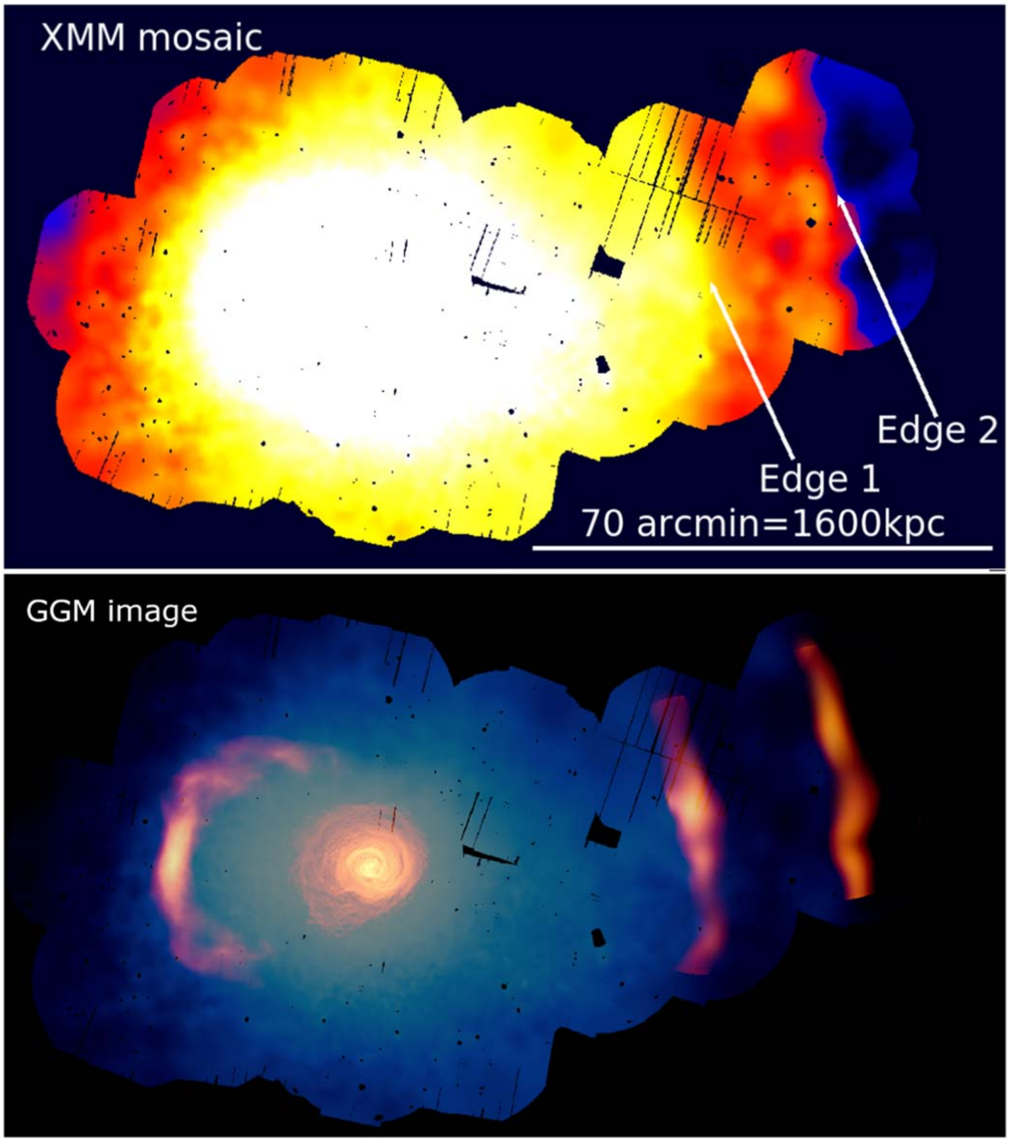

Figure 2. Top: shows the soft band (0.7–1.2 keV), background-subtracted, and exposure-corrected XMM mosaic. The two edges to the west are highlighted with arrows. Bottom: overplotting the Gaussian gradient magnitude gradient map (orange) over the normal XMM mosaic (blue) to highlight how these new edges relate to the known cold front structure in the core.

subtracted, exposure-corrected mosaic image in the 0.7–1.2 keV band is shown in the top panel of Figure 2. Two edges are clearly visible, one at 1.7 Mpc from the core and the second at 1.2 Mpc from the core, and these are labeled in the top panel of Figure 2.

To emphasize the edges, and show how they relate to the central cold fronts, we use Gaussian gradient magnitude (GGM) filtering (Sanders et al. 2016; Walker et al. 2016), which convolves the image with a Gaussian kernel and finds the gradient on the spatial scale of the kernel. The GGM-filtered image is shown in the bottom panel of Figure 2 (orange regions), where it is overlaid on the unfiltered XMM mosaic image (blue). For the central 200 kpc region we use the Chandra observations in the mosaic.

A local background field (observation 0672770101) lying beyond the virial radius ($92'$ from the core) to the east is available for a local background measurement, which is subtracted when measuring the X-ray surface brightness. When extracting surface brightness profiles in the outskirts of clusters, it is important to consider possible biases introduced by gas clumping, which become increasingly important near the virial radius (Walker et al. 2019). Eckert et al. (2015) have found that these clumping biases can be overcome by Voronoi tessellating the data and then computing the median surface brightness value in the tessellation in each radial bin.

We therefore produce a Voronoi tessellation of the XMM mosaic using the method of Diehl & Statler (2006), which is shown in Figure 3, where the image is binned so that each region contains at least 20 photons. We then extract the median surface brightness profile in a sector to the west, which is shown in Figure 6. The inferred clumping factor $\sqrt{C}$, which is the square root of the ratio of the mean deprojected surface brightness to the median deprojected surface brightness in each annulus region of the Voronoi tessellation, is plotted in the right-hand panel of Figure 3. The clumping values are relatively low, reaching up to 1.08, and consistent with those found in other works using the same technique (Eckert et al. 2015; Tchernin et al. 2016; Ghirardini et al. 2018). This

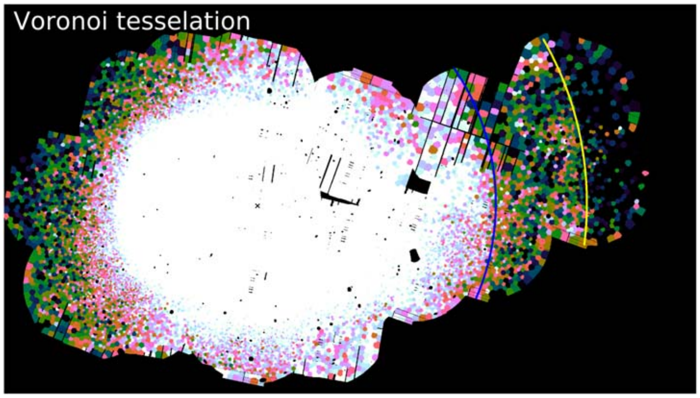

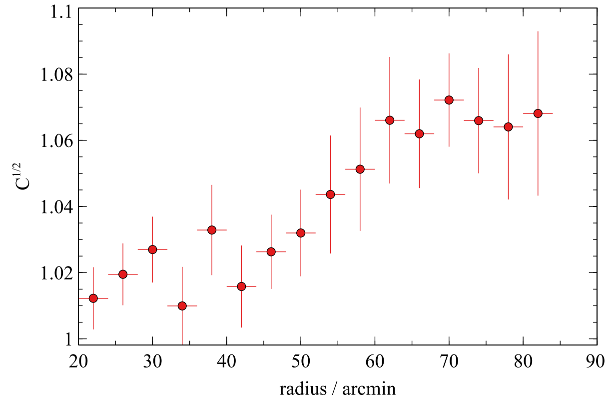

Figure 3. Left: Voronoi tessellation of the background-subtracted, exposure-corrected XMM-Newton mosaic. The locations of the two new edges are marked by the blue and yellow curves. Right: profile of the gas clumping factor inferred as the ratio between the mean and the median deprojected density in each annulus of the Voronoi tessellation.

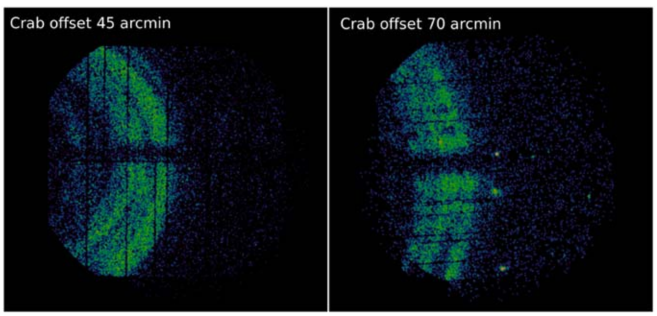

Figure 4. XMM images (the sum of the planetary nebulae and MOS detectors) in the 0.7–1.2 band at offsets of 45′ (left) and 70′ (right) from the Crab Nebula, showing the distribution of stray light.

clumping bias is therefore very mild and acts just to raise the observed densities, with no significant effect on the shape of the surface brightness profile and the magnitude of the edges we identify.

3. Stray Light

The two clear edges visible both in the images and in the median surface brightness profile are marked on Figure 2. The outermost edge lies at 1.7 Mpc from the core, just slightly smaller than the virial radius. The second edge is 1.2 Mpc from the core, and runs roughly parallel to the outer edge.

As described in the XMM-Newton User's Handbook,[5] the baffles on the X-ray telescopes of XMM-Newton reduce the effective area for stray light for observations in the range 20′–80′ from a bright source to 3 cm^2. Offset observations of the Crab Nebula have explored the spatial distribution of this stray light for a bright extended source, and found that it is spread out over arc-shaped regions of the field of view that have an area around 160 $arcmin^2$, as shown in Figure 4 for fields at 45′ and 72′ from the Crab Nebula (the obs-ids are 0122330301 and 0121910101, respectively). This spreading over a large area acts to further decrease the surface brightness of the stray light.

Estimates of the level of stray light are challenging to calculate, and subject to significant systematic errors that are poorly understood at present. Observations of the stray light from Sco-X1 have shown the stray light to vary with azimuth.[6] The values for the effective area due to stray light were obtained from ground testing of the XMM telescopes before XMM-Newton launched (de Chambure et al. 1999) and these measurements were only taken for offset angles increasing in 10′ increments (see slide 12 of this presentation; see footnote 6). It is unclear how this stray light effective area has changed over the lifetime of the XMM-Newton mission, and these ground-based measurements can only provide a rough guide. To remedy these systematic uncertainties, the best way forward is to attempt to confirm the detection of the edges with another X-ray telescope, namely ROSAT.

3.1. Comparison to ROSAT PSPC Data

In Figure 6 we compare our XMM-Newton surface brightness profile (top panel) with the profile from the same sector region of the ROSAT PSPC pointing west (middle panel). The ROSAT PSPC profiles have been renormalized to compare to the XMM data to compensate for the different collecting areas of the two instruments. The surface brightness profiles agree well. The inner edge around 1.2 Mpc arcmin is confirmed by the PSPC data. Due to the low effective area of ROSAT, the error bars of the PSPC surface brightness profile increase dramatically in the outskirts.

ROSAT's PSF increases dramatically off-axis[7] (Boese 2000), as shown by the the black exclusion circles on the left hand panel of Figure 5. The outermost edge lies toward the edge of the PSPC field of view, where the half power diameter of the ROSAT PSPC exceeds 5′ (Boese 2000). This, combined with the sparsity of counts, makes the identification of the surface brightness edge at 1.7 Mpc impossible.

4. Suzaku Spectral Analysis and Temperature Profile

The high and variable background of XMM-Newton makes it difficult to obtain reliable temperature measurements outside of r_{500} using spectral fitting. We therefore use the Suzaku data to the west (the coverage is shown by the green box in Figure 1) to obtain temperature measurements. Suzaku's low Earth orbit provided it with the low and stable background needed for accurate X-ray spectroscopy out to the virial radius.

5 https://xmm-tools.cosmos.esa.int/external/xmm_user_support/documentation/uhb/xmmstray.html

6 https://www.cosmos.esa.int/documents/332006/1301262/mjf.pdf

7 https://heasarc.gsfc.nasa.gov/docs/journal/rosat_off-axis_psf4.html

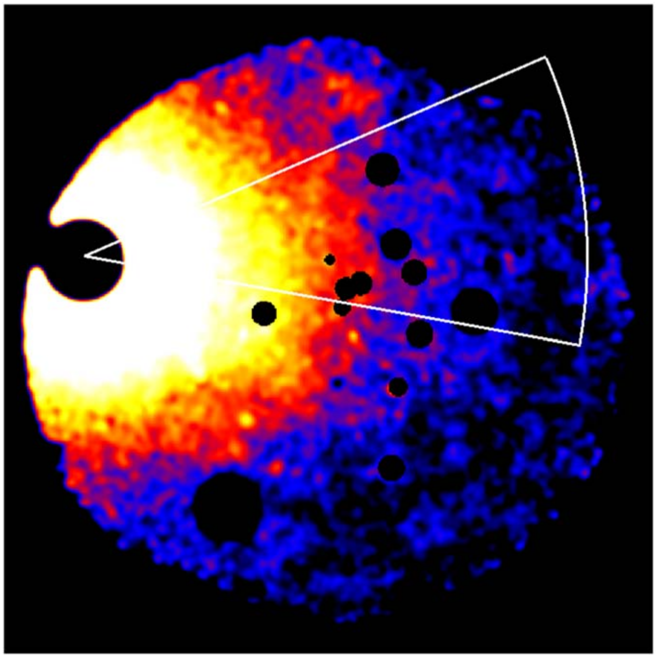

Figure 5. Left: background-subtracted and exposure-corrected ROSAT PSPC observation in the western direction, showing the same sector we use for the XMM analysis. Point sources have been removed from this image.

These data have previously been explored in Urban et al. (2014) and Simionescu et al. (2012); however, the large PSF of Suzaku prevented X-ray surface brightness edges from being measured. The Suzaku data sets in the strip to the west are tabulated in Table 2.

Our XMM-Newton data allow point sources to be identified to a much lower threshold flux than was possible in Urban et al. (2014; which just used Suzaku data), reaching down to 10^{-14} erg cm^{-2} s^{-1}. As described in Walker et al. (2013) this reduces the uncertainty in the modeling of the unresolved cosmic X-ray background. In the Suzaku spectral fitting, we follow the methods described in Walker et al. (2013), in which the contributions from the resolved point sources are included in the background model. All of the parameters in the background model were found using the outermost Suzaku data as in Urban et al. (2014). The soft X-ray background was modeled with three thermal components corresponding to the galactic halo, the local hot bubble, and a potential 0.6 keV component. The cosmic X-ray background was modeled as a power law with index 1.4 whose normalization was calculated by integrating the cumulative distribution of point sources from Moretti et al. (2003) down to the threshold flux to which we resolve point sources. To include the systematic uncertainties in the background modeling, we followed Walker et al. (2013) and performed 1000 iterations of the spectral fits, varying all of the background model parameters simultaneously through their possible ranges. The systematic uncertainty in the background model is therefore folded through and is included in the error bars shown for the temperature profile.

We extract spectra in a 6′ wide annular region (wide enough to contain sufficient photons, 1000, for a good temperature measurement), which we move along the length of the strip of Suzaku observations 1′ at a time in the regions where the edges are seen by XMM. The resulting temperature profile is shown in the bottom panel of Figure 6. We see that at each edge the temperature increases sharply as the density drops sharply, exactly what would be expected for cold fronts.

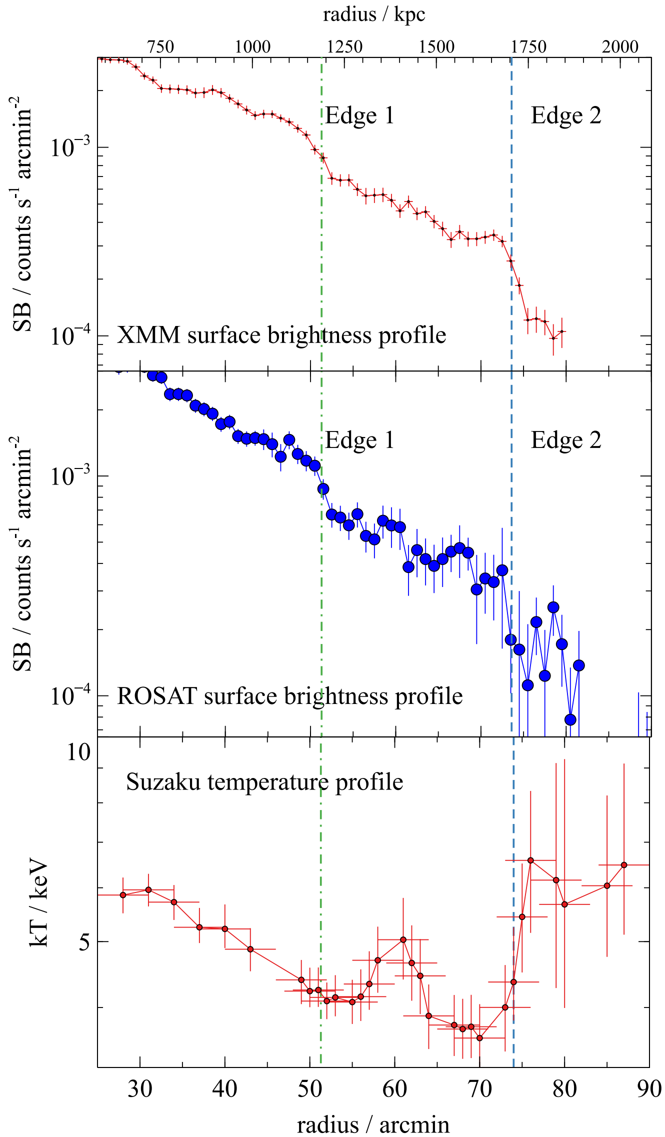

Figure 6. Top panel: projected, background-subtracted surface brightness profile from XMM-Newton, with the two edges identified. Middle panel: ROSAT PSPC surface brightness profile from the same region as the XMM-Newton surface brightness profile. The first edge at 1.2 Mpc is also seen by ROSAT; however, the data quality is insufficient to confirm the outer edge at 1.7 Mpc. The ROSAT PSPC profiles have been renormalized to compare to the XMM data to compensate for the different collecting areas of the two instruments. Bottom panel: temperature profile obtained from the Suzaku data in the same western direction as the XMM observations.

5. Comparison to Simulations

Many previous simulation studies of sloshing cold fronts have focused on the core region, given that the low-entropy dense gas in the cluster core produces the first and most obvious cold fronts that are formed (e.g., Ascasibar & Markevitch 2006; ZuHone et al. 2010, 2011, 2013, 2015; Roediger et al. 2011, 2012, 2013). However, simulations also show that cold fronts propagate to large radii at a roughly constant velocity with time (Roediger et al. 2011, 2012), as gas at these radii becomes caught up in the pattern of motions driven by the cluster merger.

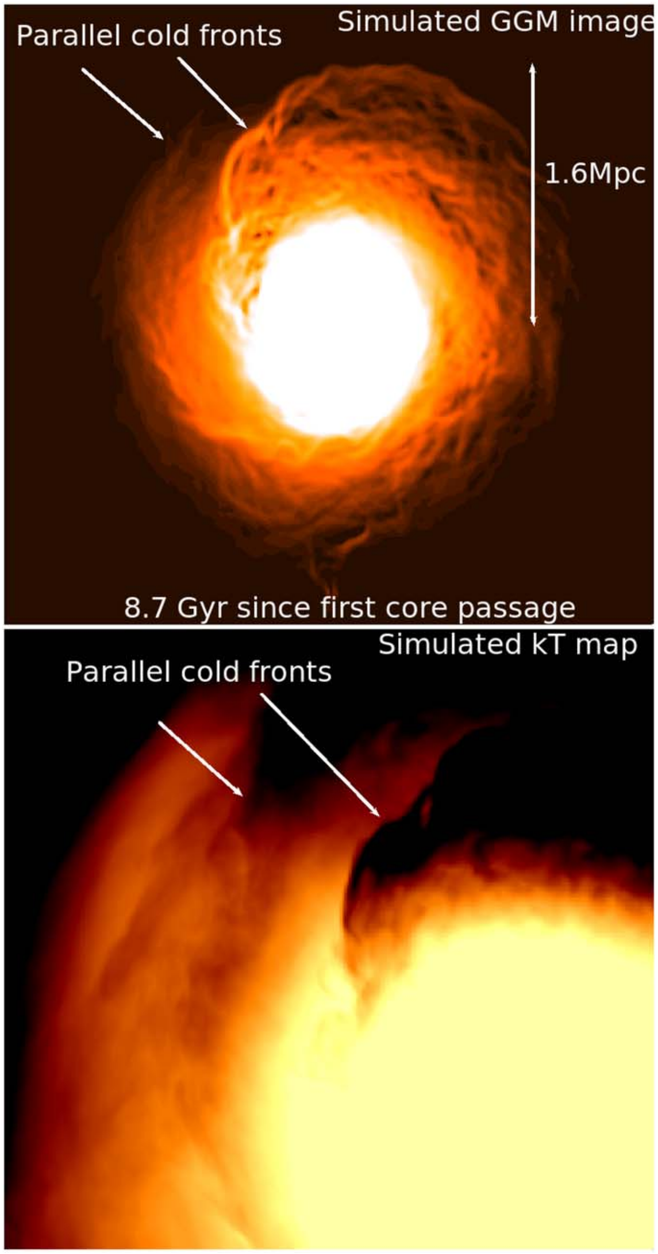

Figure 7. Top: Gaussian gradient magnitude-filtered image of the sloshing simulation 8.7 Gyr from the first core passage. We see that parallel cold fronts can form in the outskirts. In this simulation the outer cold front reaches 1.6 Mpc. Bottom: zoomed-in image of the temperature map for the parallel cold fronts in the cluster outskirts.

In Figure 7 we show the results of a simulation of a galaxy cluster merger from Brzycki & ZuHone (2019), which includes dark matter, gas, and magnetic fields. The mass ratio of this merger is $R = 3$, and the larger cluster has a mass of $M_{200} = 6 \times 10^{14}\, M_{\odot}$ (similar to the mass of the Perseus cluster of $6.6^{+0.43}_{-0.46} \times 10^{14}\, M_{\odot}$; found in Simionescu et al. 2011). Each cluster possesses a cool core and the initial ratio of thermal to magnetic pressure is $\beta = 200$. They approach each other with an initial impact parameter of $b = 1$ Mpc, which initiates large-scale gas motions that produce the cold fronts. The figure shows the state of the cluster at $t = 8.7$ Gyr past the first core passage of the subcluster. The top panel shows the GGM-filtered image of the projected X-ray emission from the cluster, revealing two cold fronts in parallel at a very large radius, up to ∼1.6 Mpc. These two cold fronts were produced shortly after core passage, near the core, and have expanded outward since, stabilized by the magnetic field despite the presence of turbulence and shock fronts. By comparison to simulations from previous works, it appears that the small mass ratio of the merger/relative large mass of the subcluster is essential to produce large cold fronts, since larger mergers produce faster gas motions that can more easily lift cold fronts to larger radii. However, the large impact parameter is also essential, since a lower impact parameter merger would destroy the core. This may indicate that the Perseus cluster underwent one of these events in the distant past. Simulations more directly tailored to the Perseus cluster will be the subject of future works.

6. Conclusions

We have analyzed new XMM-Newton observations of the western outskirts of the Perseus cluster, following up evidence from ROSAT that there is an excess in X-ray surface brightness in this direction, which appears to be due to a continuation of the gas sloshing seen in the core and around 700 kpc from the core to the east. Our main conclusions are as follows:

1. We identify two surface brightness edges in the XMM-Newton mosaic, one at 1.2 Mpc and one at 1.7 Mpc.
2. In our Suzaku spectral analysis of the same regions, there are temperature jumps at both of the edges seen in the XMM-Newton mosaic. This would be consistent with both edges being cold fronts.
3. Stray light in the XMM-Newton mosaic provides a significant systematic uncertainty that is poorly understood at present, depending in a nontrivial way on the roll angle of the observations. When we explore ROSAT PSPC data for the same region as that explored by XMM-Newton, we find that the inner edge at 1.2 Mpc is also seen by ROSAT. However, due to the limitations of the ROSAT PSPC data, the outer edge at 1.7 Mpc cannot be confirmed.
4. At present, the systematic uncertainties in the level of stray light in the XMM-Newton observations mean we cannot determine whether the outer edge at 1.7 Mpc is definitively a cold front, or whether this feature is the result of stray light (in which case the temperature jump seen by Suzaku in this region would just be a coincidence).
5. We also use a numerical simulation of a binary galaxy cluster merger to show that such cold fronts can indeed be produced by sloshing motions in the core and expand outward to large radii, stabilized against turbulence by magnetic fields. The formation of these large fronts appears to require a large impact parameter and low-mass ratio mergers, which can drive fast gas motions without destroying the core completely.

We thank the referee for helpful comments that improved the paper. S.A.W. and M.S.M. acknowledge support from the NASA XMM-Newton grant No. 80NSSC19K1698. Based on observations obtained with XMM-Newton, an ESA science mission with instruments and contributions directly funded by ESA Member States and NASA.

Appendix
Observations Used

Table 1
XMM Data Used in This Paper Ordered by Date Taken

Obs ID	R.A.	Decl.	Start Date	Exposure (ks)	Distance from Core (arcmin)
0820720401	03 13 29.22	+41 53 08.7	2019-03-04	28.8	74.01
0820720301	03 13 16.44	+41 35 51.8	2019-02-26	25.0	73.28
0820720201	03 15 26.68	+41 45 05.4	2019-02-24	25.3	50.74
0820720101	03 15 16.88	+41 24 17.2	2019-02-20	25.4	51.06
0673020401	03 21 14.16	+41 10 52.3	2012-03-01	31.9	25.75
0673020201	03 23 07.63	+41 12 35.6	2011-09-10	39.0	41.78
0673020301	03 22 10.00	+41 23 00.0	2011-08-19	35.9	27.87
0672770101	03 28 00.10	+41 29 56.5	2011-08-04	16.9	92.28
0554500801	03 25 25.20	+40 46 23.6	2008-08-19	34.1	77.59
0405410101	03 21 04.26	+41 56 05.0	2006-08-03	30.9	28.72
0405410201	03 18 39.93	+41 06 31.4	2006-08-03	34.0	27.35
0305690301	03 19 50.59	+41 53 34.3	2006-02-11	27.2	22.8
0305690401	03 21 53.70	+41 49 30.1	2006-02-11	27.9	30.14
0305690101	03 18 02.69	+41 16 60.0	2006-02-10	27.9	23.96
0305780101	03 19 48.00	+41 30 40.7	2006-01-29	125	0.18
0306680301	03 13 01.97	+41 20 01.2	2005-09-04	63.4	76.72
0305720101	03 17 57.99	+41 45 57.0	2005-09-01	21.8	25.42
0305720301	03 22 15.99	+41 11 28.0	2005-08-03	28.3	33.95
0204720201	03 23 23.60	+41 31 41.0	2004-02-04	24.9	40.52
0204720101	03 21 38.59	+41 31 43.0	2004-02-04	17.9	20.87
0151560101	03 16 42.99	+41 19 29.0	2003-02-26	29.4	36.33
0002942401	03 15 01.40	+42 02 09.0	2002-01-28	7.9	61.83
0085590201	03 19 49.69	+41 05 47.0	2001-02-10	43.3	25
0085110101	03 19 48.16	+41 30 42.1	2001-01-30	60.8	0.2

Note. The four observations taken in 2019 extend the coverage of the mosaic to the west and are the focus of this paper.

Table 2
Suzaku Data Used in This Paper

Obs ID	R.A.	Decl.
805117010	47.1647	41.6449
805109010	47.3511	41.6379
805116010	47.5391	41.63
805108010	47.7251	41.6255
805115010	47.9127	41.6204
805107010	48.1001	41.6131
805114010	48.2846	41.6054
805106010	48.4696	41.6016
805105010	48.8462	41.5856
805104010	49.2188	41.5721
805103010	49.5928	41.5523

ORCID iDs

S. A. Walker https://orcid.org/0000-0002-6413-4142
M. S. Mirakhor https://orcid.org/0000-0002-7595-6723
J. ZuHone https://orcid.org/0000-0003-3175-2347
J. S. Sanders https://orcid.org/0000-0003-2189-4501
A. C. Fabian https://orcid.org/0000-0002-9378-4072

References

Asai, N., Fukuda, N., & Matsumoto, R. 2007, ApJ, 663, 816
Ascasibar, Y., & Markevitch, M. 2006, ApJ, 650, 102
Boese, F. G. 2000, A&AS, 141, 507
Brzycki, B., & ZuHone, J. 2019, ApJ, 883, 118
de Chambure, D., Lainé, R., van Katwijk, K., & Kletzkine, P. 1999, ESABu, 100, 30
Diehl, S., & Statler, T. S. 2006, MNRAS, 368, 497
Douglass, E. M., Blanton, E. L., Randall, S. W., et al. 2018, ApJ, 868, 121
Dursi, L. J. 2007, ApJ, 670, 221
Eckert, D., Roncarelli, M., Ettori, S., et al. 2015, MNRAS, 447, 2198
Ghirardini, V., Ettori, S., Eckert, D., et al. 2018, A&A, 614, A7
Lau, E. T., Kravtsov, A. V., & Nagai, D. 2009, ApJ, 705, 1129
Lyutikov, M. 2006, MNRAS, 373, 73
Markevitch, M., & Vikhlinin, A. 2007, PhR, 443, 1
Moretti, A., Campana, S., Lazzati, D., & Tagliaferri, G. 2003, ApJ, 588, 696
Roediger, E., Brüggen, M., Simionescu, A., et al. 2011, MNRAS, 413, 2057
Roediger, E., Kraft, R. P., Forman, W. R., Nulsen, P. E. J., & Churazov, E. 2013, ApJ, 764, 60
Roediger, E., Lovisari, L., Dupke, R., et al. 2012, MNRAS, 420, 3632
Rossetti, M., Eckert, D., De Grandi, S., et al. 2013, A&A, 556, A44
Sanders, J. S., Dennerl, K., Russell, H. R., et al. 2020, A&A, 633, A42
Sanders, J. S., Fabian, A. C., Russell, H. R., Walker, S. A., & Blundell, K. M. 2016, MNRAS, 460, 1898
Simionescu, A., Allen, S. W., Mantz, A., et al. 2011, Sci, 331, 1576
Simionescu, A., Werner, N., Urban, O., et al. 2012, ApJ, 757, 182
Snowden, S. L., Mushotzky, R. F., Kuntz, K. D., & Davis, D. S. 2008, A&A, 478, 615
Tchernin, C., Eckert, D., Ettori, S., et al. 2016, A&A, 595, A42
Tittley, E. R., & Henriksen, M. 2005, ApJ, 618, 227
Urban, O., Simionescu, A., Werner, N., et al. 2014, MNRAS, 437, 3939
Walker, S., Simionescu, A., Nagai, D., et al. 2019, SSRv, 215, 7
Walker, S. A., Fabian, A. C., & Sanders, J. S. 2014, MNRAS, 441, L31
Walker, S. A., Fabian, A. C., Sanders, J. S., Simionescu, A., & Tawara, Y. 2013, MNRAS, 432, 554
Walker, S. A., Hlavacek-Larrondo, J., Gendron-Marsolais, M., et al. 2017, MNRAS, 468, 2506
Walker, S. A., Sanders, J. S., & Fabian, A. C. 2016, MNRAS, 461, 684
Walker, S. A., ZuHone, J., Fabian, A., & Sanders, J. 2018, NatAs, 2, 292
ZuHone, J. A., Kunz, M. W., Markevitch, M., Stone, J. M., & Biffi, V. 2015, ApJ, 798, 90
ZuHone, J. A., Markevitch, M., & Johnson, R. E. 2010, ApJ, 717, 908
ZuHone, J. A., Markevitch, M., & Lee, D. 2011, ApJ, 743, 16
ZuHone, J. A., Markevitch, M., Ruszkowski, M., & Lee, D. 2013, ApJ, 762, 69
Zuhone, J. A., & Roediger, E. 2016, JPlPh, 82, 535820301